Optimization of a Protocol for Visualizing Vascular and Cellular Pore Networks in Human Bone Using Multiphoton Confocal Microscopy

Mary Cole, M.A.
Advisor: Dr. Samuel D. Stout
Department of Anthropology, The Ohio State University
The 31st Edward F. Hayes Graduate Research Forum

ABSTRACT

Biological anthropologists measure changes in bone mass to make inferences about patterns of physical activity in the past. Bone is resorbed in response to low strain, and added in response to high strain[29,30]. By measuring the typical amount and distribution of bone mass in a population, anthropologists can approximate how different bones were typically bent. They further infer physical behaviors that could have caused this bending pattern in the past population, commonly including subsistence, mobility, terrain, type of transportation, and tool use[31]. About 70% of age-related bone loss in appendicular bones occurs in the cortical "wall" of bone. This is mostly due to the formation of vascular pores within the cortex, a factor not typically considered in analysis of bone mass[1]. If anthropologists knew how mechanical strain changes affected the formation and structure of pore systems, they could use pore structures to infer trends in physical behavior too subtle to affect overall bone shape. Vascular pores also concentrate stress, such that microscopic damage initiates and spreads within pore systems, leading to bone fracture[7]. Understanding how vascular pore systems enlarge could help clinical researchers to regulate pore-producing cellular processes in pathological bone loss such as osteoporosis.

The relationship between mechanical strain and three-dimensional pore structure is poorly understood due to historical reliance on two-dimensional imaging methods. Pore numbers and sizes are distorted in two-dimensional cross-section by frequent splitting and merging of pore systems[13,14]. Theoretically, vascular pores should be formed to help remove bone under low

strains[8]. Yet two-dimensional methods have produced many contradictory inferences about the relationship of pore number and orientation to mechanical demand[13,32]. A separate cellular (lacunar-canalicular) pore network houses osteocyte cells, which trigger bone formation or resorption in response to mechanical strain changes or microdamage[10]. Cellular pores should theoretically predominate in regions under high strain, where the cells are needed to detect damage. Yet two-dimensional methods can only count the number of these tiny lacunae and have not produced consistent associations with mechanical demand[33].

We sought to optimize a three-dimensional imaging protocol for visualizing vascular and cellular pore networks in human bone. Confocal laser scanning microscopy (CLSM) is an emerging method for three-dimensional imaging of bone tissue, with higher resolution than more traditional micro-CT. Multiphoton CLSM uses two photons of infrared light to excite a fluorescent stain in a bone structure at a precise >1 μm diameter location and depth[25]. Successive depths are stacked into a three-dimensional image[20]. Current methods of staining human bone porosity for CLSM imaging use decalcification that can introduce histological defects[12,18,19], or require perfusion of a stain during life[20], or stain non-pore features[21].

Ciani *et al.*[22] developed a staining protocol for rats and mice, using fluorescein isothiocyanate isomer I (FITC) at 1% in 100% ethanol to exclusively stain vascular and cellular pores. However, rats and mice lack the large vascular pore systems seen in humans[26]. We tested this protocol for visualizing vascular and cellular pore networks in human bone. Ten cross-sections approximately 500 to 600 μm in thickness were cut from the midshaft of a fresh cadaveric human rib. Each cross-section was placed in a 15 mL volume of freshly prepared 4% formaldehyde and fixed for 24 hours at room temperature under gentle rotation. Cross-sections were dehydrated in ascending grade ethanol (75%, 95%, and 100% for 5 minutes each). FITC

was diluted in 100% ethanol at concentrations of 1%, 0.9%, 0.8%, 0.7%, 0.6%, 0.5%, 0.4%, 0.2%, and 0.1%. Each 10 mL solution was gently rotated for one hour and then filtered. Each cross-section was placed in a different concentration of solution for four hours under gentle rotation. Each cross-section was then rinsed in 15 mL of 100% ethanol under gentle rotation for 30 minutes, and then air dried. Small regions (508.93 µm x 508.93 µm) were imaged using an Olympus FV1000 MPE Multiphoton Laser Scanning Confocal microscope with N.A. 1.05, 25x water immersion objective, 800 nm laser excitation wavelength, resolution 1024 x 1024 pixels, step size 0.63 µm, and 2x Kalman averaging.

Stain concentrations above 0.5% FITC could clearly resolve vascular and cellular pore structures approximately 100 µm deep into the sample (1% = 150.81 µm, 0.9% = 104.26 µm, 0.8% = 122.32 µm, 0.7% = 129.97 µm, 0.6% = 142.65 µm). As stain concentration fell below 0.5%, depth of penetration dropped off sharply (0.5% = 76.86 µm, 0.4% = 66.15 µm, 0.3% = 76.23 µm, 0.2% = 59.04 µm, 0.1% = 59.85 µm). As concentration decreased from 1% FITC, pore structures also became more variable in brightness at a given depth in the sample. The high voltage and offset values required to visualize the smaller cellular pores sacrificed resolution at the boundaries of the vascular pores, which were much brighter due to greater stain absorption.

INTRODUCTION

Forensic Relevance of Porosity: Bone Fragility and Fracture Risk

About 70% of age-related bone loss in limbs occurs within the cortex, mostly due to the formation of vascular pores that carry blood vessels[1]. At least 76% of the reduction in cortical strength with age results from vascular porosity[2]. These pores initially form during the remodeling processes that renew bone throughout life. Osteoclast cells tunnel into old or damaged bone and osteoblast cells fill this tunnel with new bone, leaving a central vascular pore to conduct a blood vessel[3]. Yet osteoblasts' capacity for bone formation slows with age. They cannot keep pace in filling the resorbed spaces, which accumulate as large pores called resorption bays[4]. Lowered mechanical strains, such as declining physical activity and weakening muscles, trigger further resorption to expand, connect, and "trabecularize" existing pores[5,6]. Vascular pores compromise mechanical strength because they concentrate stress. Microscopic cracks ("microdamage") that form within a pore system can propagate through these highly interconnected tunnels until the bone fractures[7]. Vascular porosity serves as a marker of bone fragility and fracture risk, both in a biomedical context and for assessing the likelihood of accidental fracture in a forensic context.

Anthropological Relevance of Porosity: Mechanical Loading History

Pore distribution and shape (Fig. 1) may record a bone's mechanical loading history, allowing inference of bone use, such as physical activity patterns. Vascular porosity accumulates in regions under low mechanical strain[8,9]. A separate cellular pore network may expand under high mechanical strain. The cellular pore network includes spherical lacunae, each containing an osteocyte cell body, and fluid-filled canaliculi, which connect osteocytes through their ~50 dendritic processes[10]. Osteocytes trigger bone resorption and remodeling in response to local

mechanical strain change and microscopic damage, so they may be more active in high-strain regions. Loaded bones have been found to have larger lacunar volumes and more branched canaliculi compared to unloaded bones[11,12].

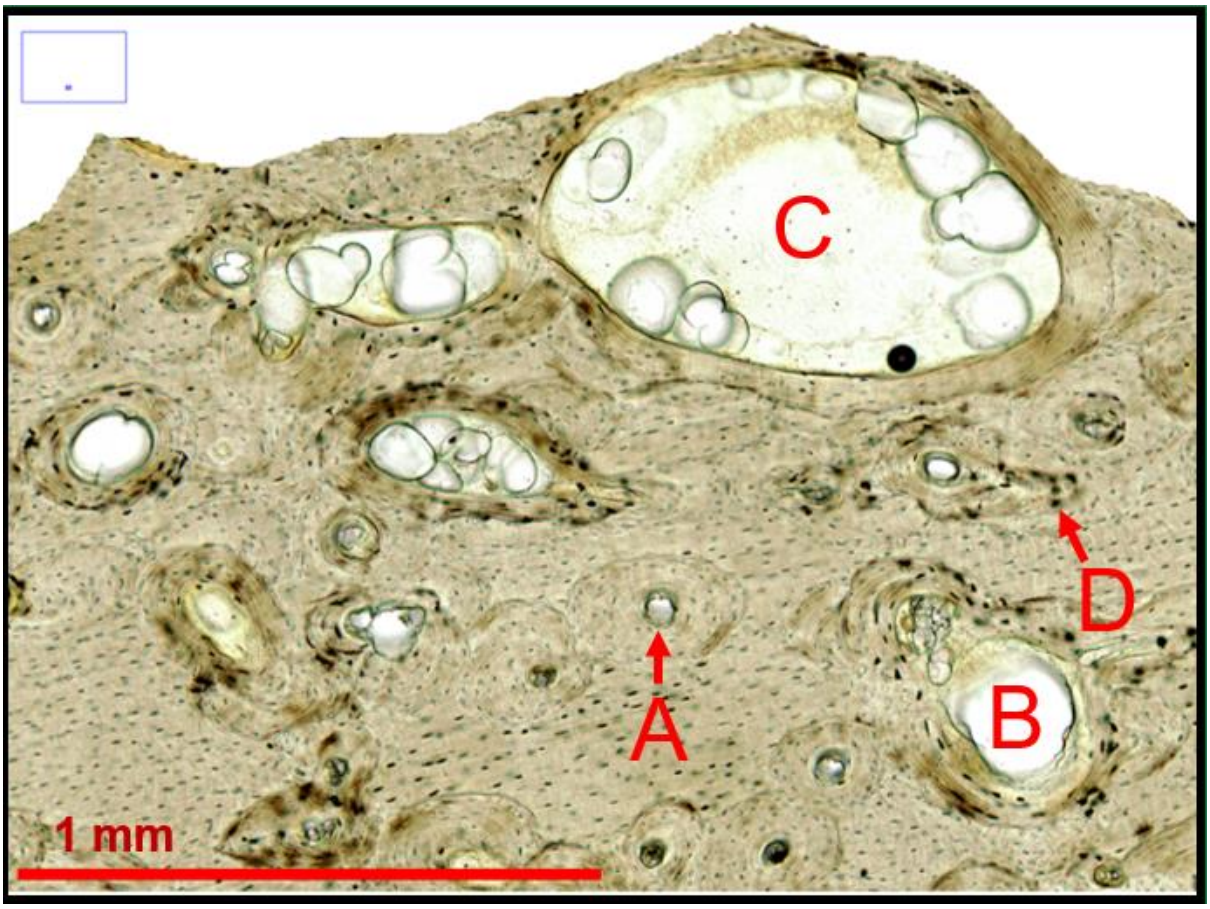

Figure 1. 2D Cross-Section of Pore Types in Human Bone. [A] Finished vascular pore (Haversian canal) [B] Unfinished vascular pore (Resorption bay) [C] Coalesced vascular pore (Trabecularized) [D] Osteocyte Lacuna (Canaliculi Not Visible)

Limitations of Current Pore Imaging Methods

Three-dimensional vascular and cellular pore structures remain largely unstudied, especially in terms of variation between bone regions or changes with age. Extrapolations from two-dimensional studies are often contradictory. Pore systems frequently merge, split, and

interconnect, and can be obliquely oriented to the plane of sectioning, distorting their true dimensions in two-dimensional cross-section[13-16]. In bone, imaging technologies that rely on X-rays (microCT) or epi-illumination (widefield fluorescence microscopy) have limited imaging depth and resolution. Mineralized bone has a high refractive index and strongly absorbs or scatters the light that must pass through its tissue to the detector[16,17].

Confocal laser scanning microscopy (CSLM) is an emerging alternative for higher resolution three-dimensional imaging of bone. Several studies have applied single-photon CLSM to small regions of bone tissue, thereby visualizing vascular pores, lacunae, and canaliculi[19-25]. Ciani et al. (2009)[23] stained rat tibiae with fluorescein isothiocyanate isomer I (FITC) at 1% in 100% ethanol and imaged all cellular pore networks in a two-dimensional plane with single-photon CSLM. This study optimizes this staining protocol and tests image thresholding for multiphoton (two-photon) CSLM in order to visualize three-dimensional complex pore networks in human bone.

MATERIALS AND METHODS

How Does CSLM Create 3D Images?

Widefield fluorescence microscopy uses a scanning laser to excite a fluorophore attached to a structure of interest. This fluorophore emits light, which travels back through the tissue and is sensed by a photomultiplier (PMT) detector, creating an image of the structure of interest. Yet fluorophores in out-of-focus regions also emit light, blurring the structure that is in focus. Single-photon CSLM uses a spinning disk or a pinhole to block this out-of-focus fluorescent light, allowing clearer visualization of the fluorophore in the X, Y, and Z (depth) planes. The two-dimensional depths taken in each Z-plane are stacked into a three-dimensional image[26].

Multiphoton CLSM (Fig. 2) uses a near-infrared laser to emit two low-energy photons, which are absorbed simultaneously at a precise coordinate and depth in the tissue. Only that specific point emits a single photon, so no out-of-focus fluorescent light interferes. The infrared laser is absorbed and scattered by tissue less than visible light, allowing penetration up to 800 µm[26].

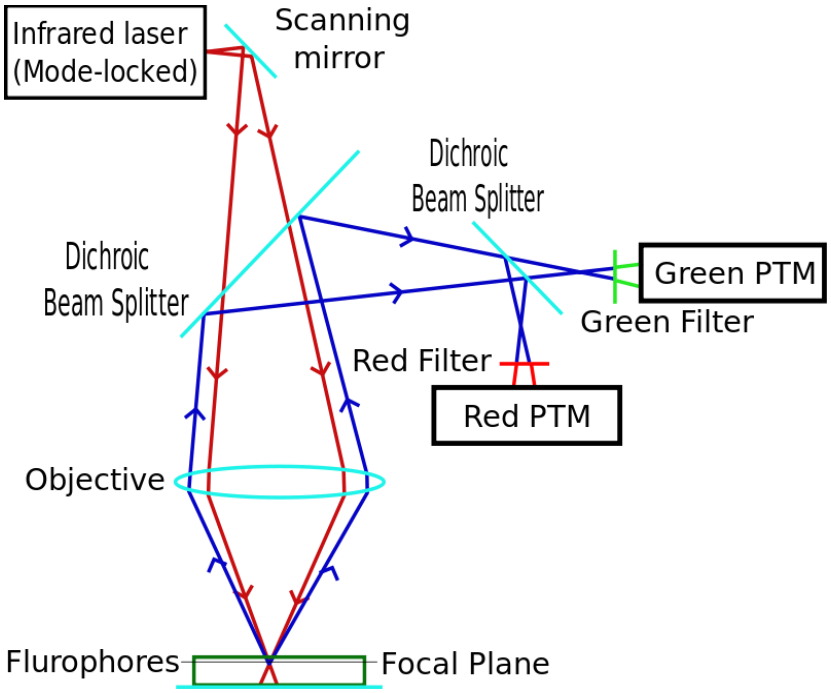

Figure 2. Light pathways in multiphoton confocal laser scanning microscopy[34]

Need for Optimization

Ciaini et al.'s[22] staining protocol was chosen for this study because it only stains pore spaces, and has visualized lacunar-canalicular networks in two-dimensional cross-section. In our initial pilot of the 1% FITC concentration, and in its repeat shown below (Fig. 3), vascular pores in human bone absorbed too much of the FITC stain, obscuring adjacent structures. Rats and mice, used in the original protocol, do not usually have vascular Haversian canals[27]. This study tests the penetration and visibility of stain concentrations in 0.1% increments from 1% FITC to 0.1% FITC.

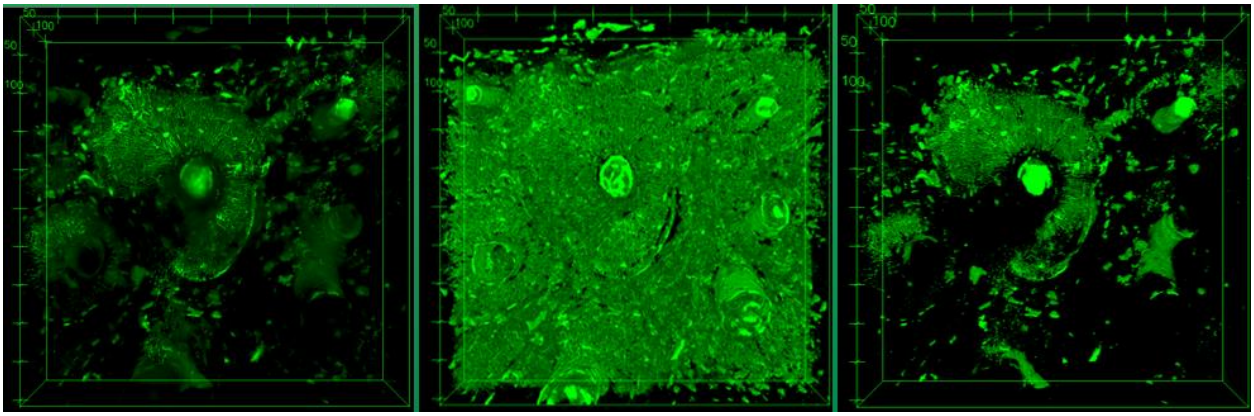

1% - Original Image **1% - Auto Local Threshold** **1% - BoneJ Optimise**

Figure 3. Vascular and cellular pore structures stained with 1% FITC Concentration

Staining Protocol Derived from Ciani et al.[22]

Ten cross-sections ~ 500 to 600 µm in thickness were cut from the midshaft of a fresh cadaveric human left fourth rib. Each cross-section was placed in a 15 mL volume of freshly prepared 4% formaldehyde and fixed for 24 hours at room temperature under gentle rotation. Cross-sections were dehydrated in ascending grade ethanol (75%, 95%, and 100% for 5 minutes each). FITC was diluted in 100% ethanol at concentrations of 1%, 0.9%, 0.8%, 0.7%, 0.6%, 0.5%, 0.4%, 0.2%, and 0.1%. Each 10 mL solution was gently rotated for one hour and then filtered. Each cross-section was placed in a different concentration of solution for four hours under gentle rotation. Each cross-section was then rinsed in 15 mL of 100% ethanol under gentle rotation for 30 minutes, and then air dried.

Sample Imaging

Small regions of each cross-section were imaged using an Olympus FV1000 MPE Multiphoton Laser Scanning Confocal microscope with N.A. 1.05, 25x water immersion objective, 800 nm laser excitation wavelength, resolution 1024 x 1024 pixels, and step size 0.63 µm. Frames were imaged twice with Kalman averaging to improve signal to noise (S/N) ratio. Laser intensity was minimized to prevent photobleaching of the fluorescent stain. To optimize

image intensity by using the full dynamic range of the detector, gain (High Voltage or HV) and offset were adjusted with increasing depth within the sample. Increasing HV multiplies the output signal to increase its brightness. Offset adds positive or negative voltage to low output signals (dark areas) of the image, making them brighter or darker[26].

Image Processing

Each image stack was loaded into the image analysis software FIJI , an ImageJ distribution, and visualized in the ImageJ 3D Viewer[28]. Two three-dimensional thresholding methods were tested to extract pore objects from the background by converting them to binary images. The Auto Local Threshold plugin[28] thresholds each pixel on each image slice based on the Otsu threshold (which minimizes intra-class variance) of a surrounding radius of pixels. Otsu's method was used in a previous two-dimensional application of this protocol to rat tibia lacunar-canalicular pore networks[24]. The BoneJ Optimise Threshold plugin[29] thresholds an image stack based on a histogram of all pixels in the stack.

RESULTS

An optimal stain concentration should resolve the smallest structures of interest, which are canaliculi in the case of porosity. Vascular pores are large, ranging from a 50-80 μm diameter for Haversian canals to a 150 – 300 μm diameter for resorption bays. Cellular pores include a ~10 μm lacuna and 0.1 to 1 μm diameter canaliculi[3]. For this protocol, maximum depth refers to the deepest point in the bone tissue where canaliculi could still be distinguished from the background. The imaged depth used to generate 3D images was set where the majority of pore structures in the field of view could be resolved. For stain concentrations of 0.6% to 1%, canaliculi were distinct even at maximum depths ranging from 100 to 150 μm. This resolution dropped off sharply for stain concentrations of 0.5% to 0.1% (Fig. 4, Table 1).

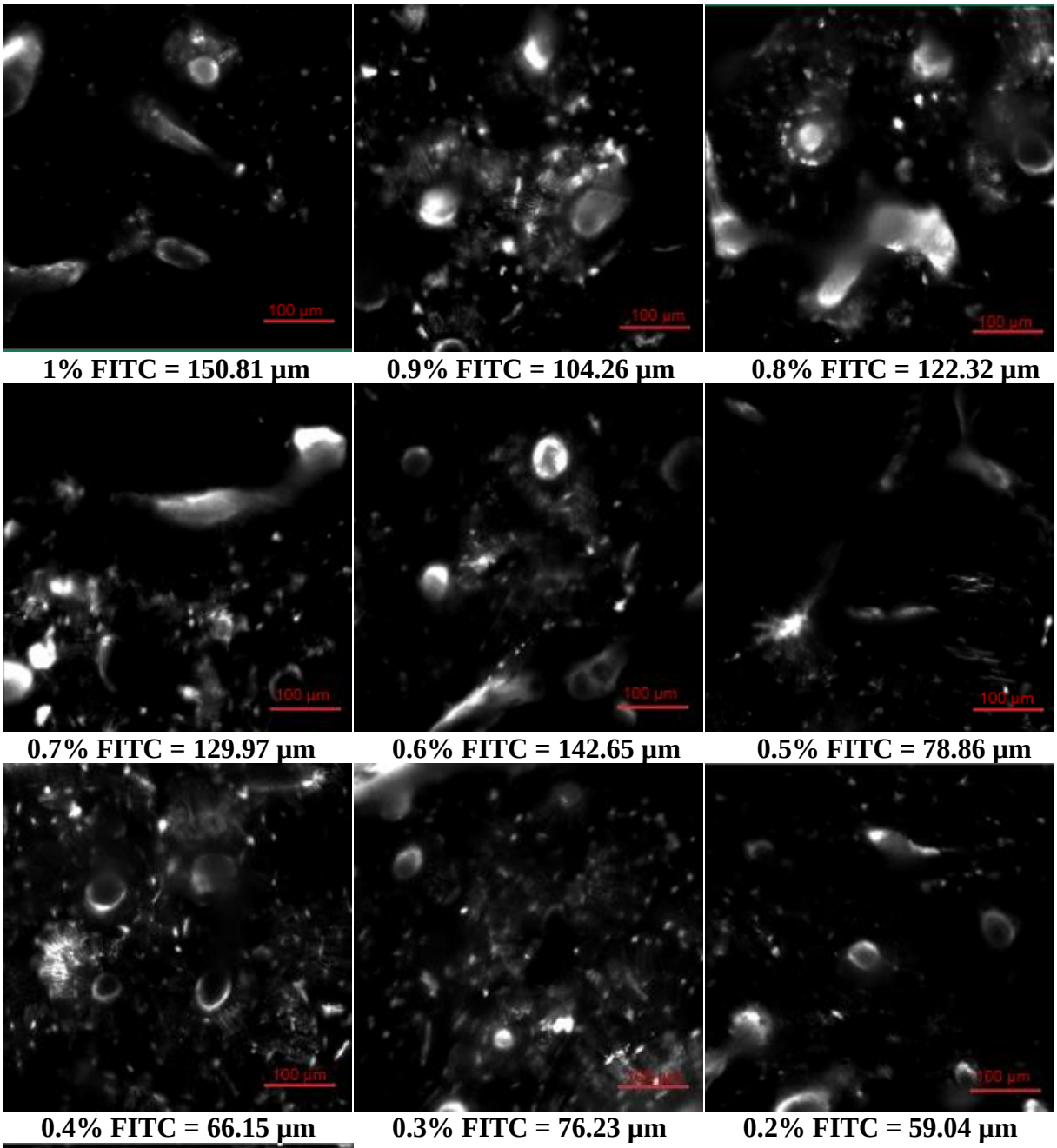

1% FITC = 150.81 µm **0.9% FITC = 104.26 µm** **0.8% FITC = 122.32 µm**

0.7% FITC = 129.97 µm **0.6% FITC = 142.65 µm** **0.5% FITC = 78.86 µm**

0.4% FITC = 66.15 µm **0.3% FITC = 76.23 µm** **0.2% FITC = 59.04 µm**

0.1% FITC = 59.85 µm

Figure 4: Maximum depth of penetration, with resolvable canaliculi, for FITC stain concentrations from 1% to 0.1%

Stain %	Imaged Depth (µm)	Maximum Depth (µm)
1%	105.21	**150.81**
0.9%	64.89	**104.26**
0.8%	85.05	**122.32**
0.7%	99.54	**129.97**
0.6%	99.54	**142.65**
0.5%	76.86	76.86
0.4%	66.15	66.15
0.3%	76.23	76.23
0.2%	44.1	**59.04**
0.1%	59.85	59.85

Table 1: Image depths incorporated in three-dimensional structure, compared to maximum resolvable depth of penetration, for FITC stain concentrations from 1% to 0.1%. Bolding indicates the maximum depth exceeds the imaged depth.

FITC concentrations between 0.6% and 1% resolved the smallest pore structures, canaliculi, at depths of 100 to 150 µm. As FITC concentrations decreased, large vascular pores, which absorb more stain, increased in brightness relative to lacunae and canaliculi. To visualize these smaller and dimmer structures, mid- and low FITC concentrations required rapid increases in gain (HV) and offset with increasing depth (Fig. 5). Increasing HV also increases noise in the image, while increasing offset can eliminate the dark areas of the image that demarcate feature boundaries[25].

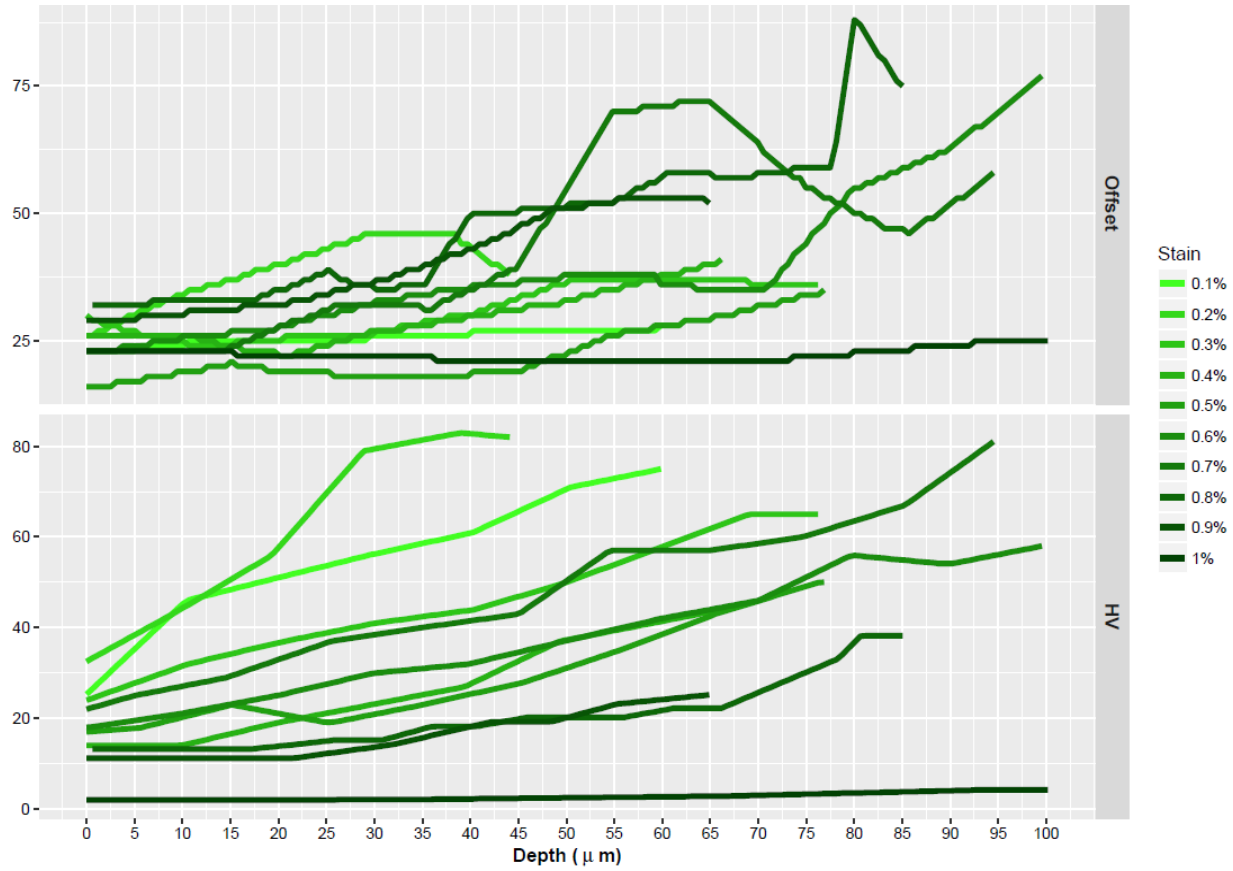

Figure 5. At lower FITC concentrations, resolution of pore structures requires rapid increases of gain (HV) and offset with increasing depth of penetration into the sample.

The thresholding method determined how this deterioration of feature boundaries altered the structure of pore networks visible in each individual two-dimensional slice (Figs. 6) and in each three-dimensional image composed of the stacked two-dimensional slices (Fig. 7-9). In the original, non-thresholded image, the fine structures of the canaliculi were distorted by increased image noise and the disappearance of their dark boundaries. Adjacent canaliculi and lacunae were blurred into large masses. The auto local threshold method thresholds each pixel based on the gray level of a radius of adjacent pixels, so the linear structure of the canaliculi was preserved. However, adjacent pixels representing image noise were increasingly incorporated, artificially expanding and thickening these cellular pore networks. The BoneJ Optimise

Threshold method determines the image threshold using a histogram of all pixels in an image stack. To reduce the chance of false connections created by image noise, this method minimizes connectivity with a “purify” step that filters out small foreground and background particles. Canaliculi were pruned from lacunae if they were isolated. Cellular networks were retained as large masses if they merged with each other or a vascular pore.

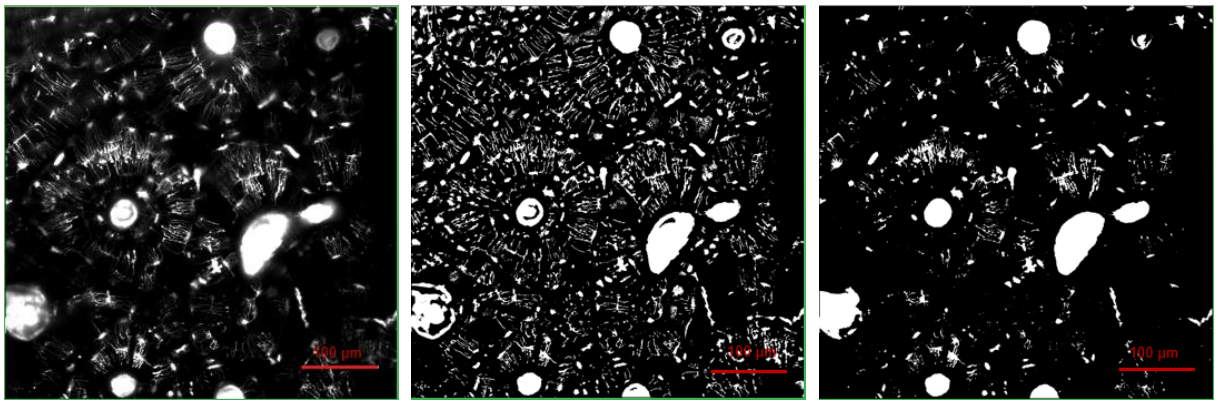

Original Image **Auto Local Threshold** **BoneJ Optimise**

Figure 6: Two-dimensional slice closest to the surface of the bone in each thresholding method, demonstrated on the 0.9% FITC sample

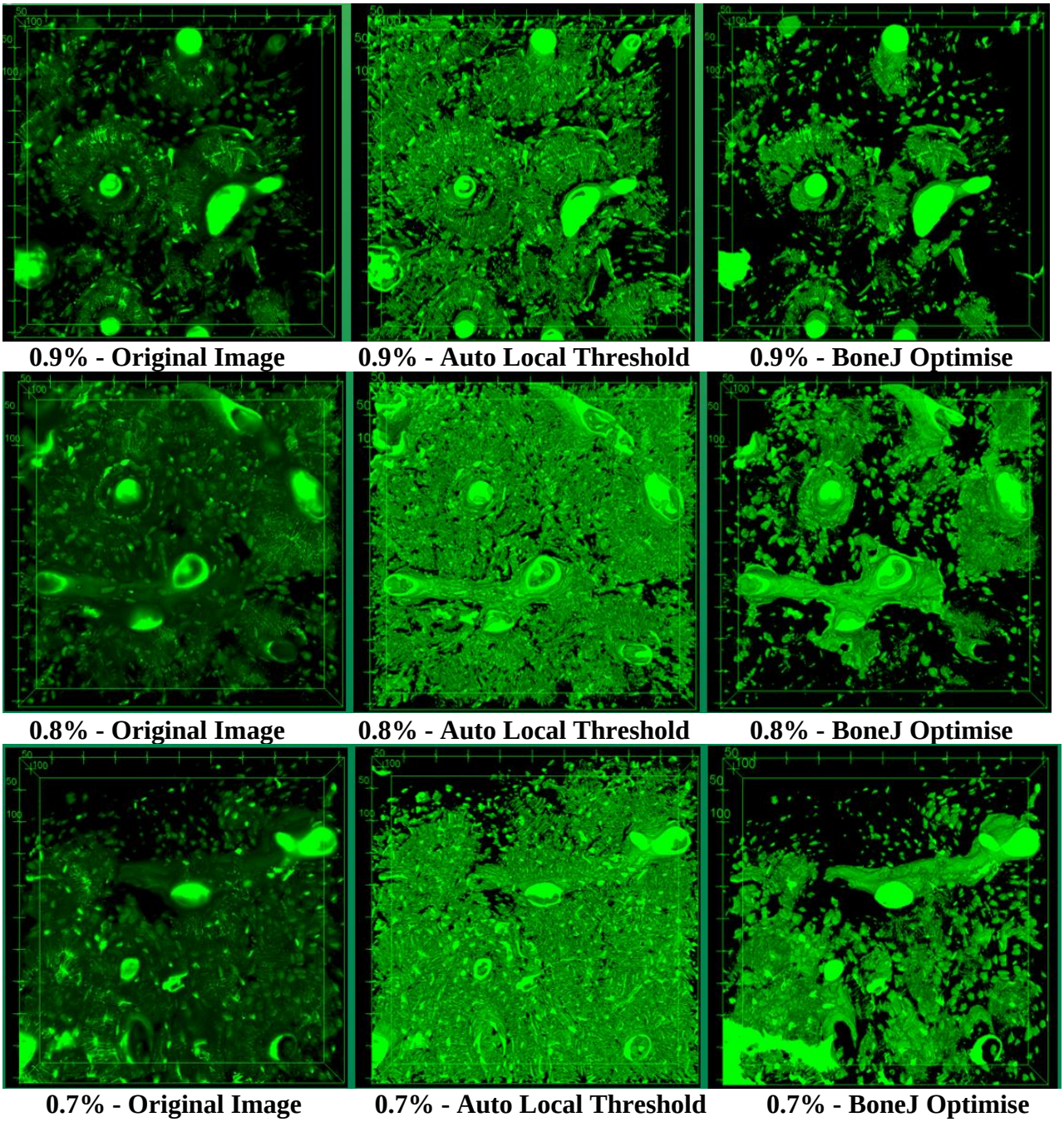

Figure 7: Three-dimensional images with each thresholding method for 0.9% - 0.7% FITC

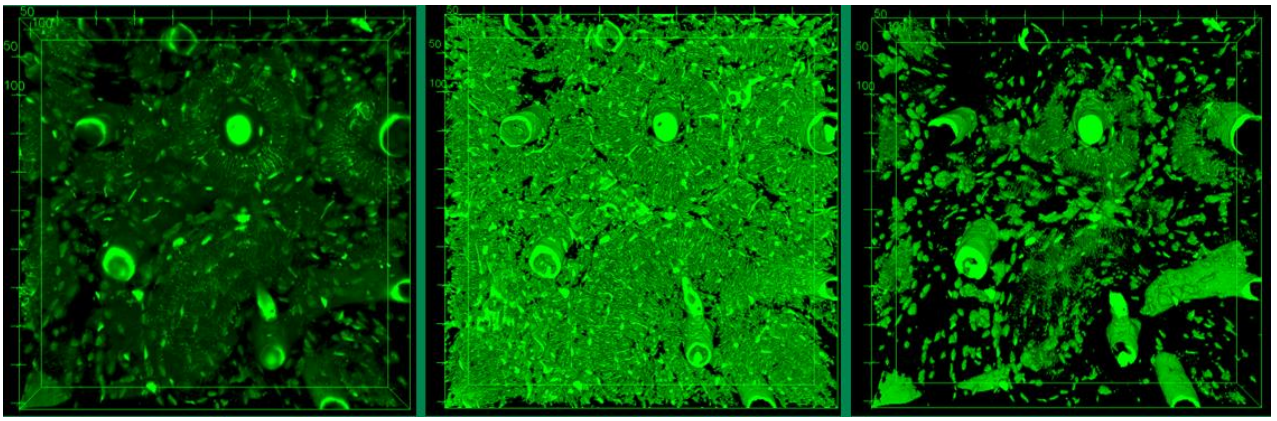

0.6% - Original Image **0.6% - Auto Local Threshold** **0.6% - BoneJ Optimise**

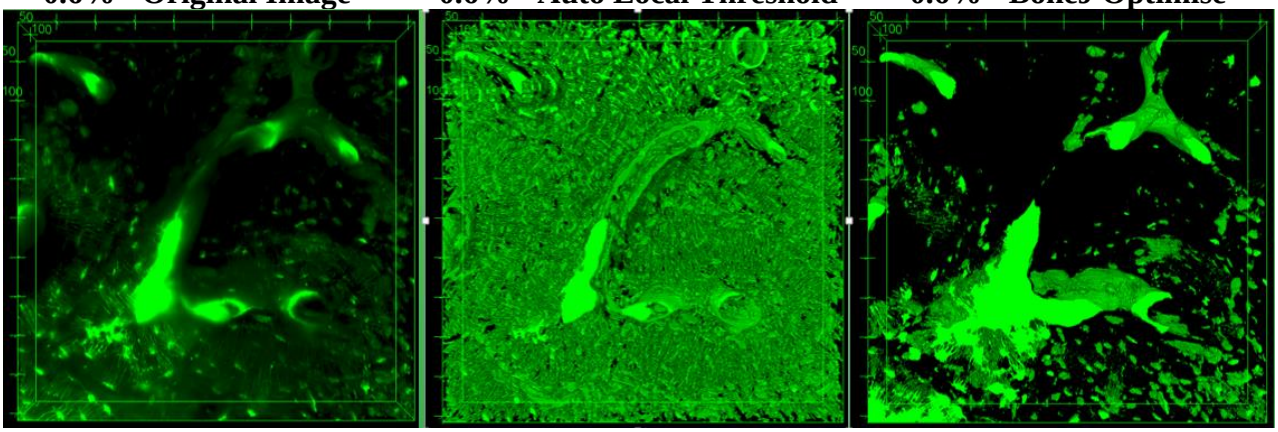

0.5% - Original Image **0.5% - Auto Local Threshold** **0.5% - BoneJ Optimise**

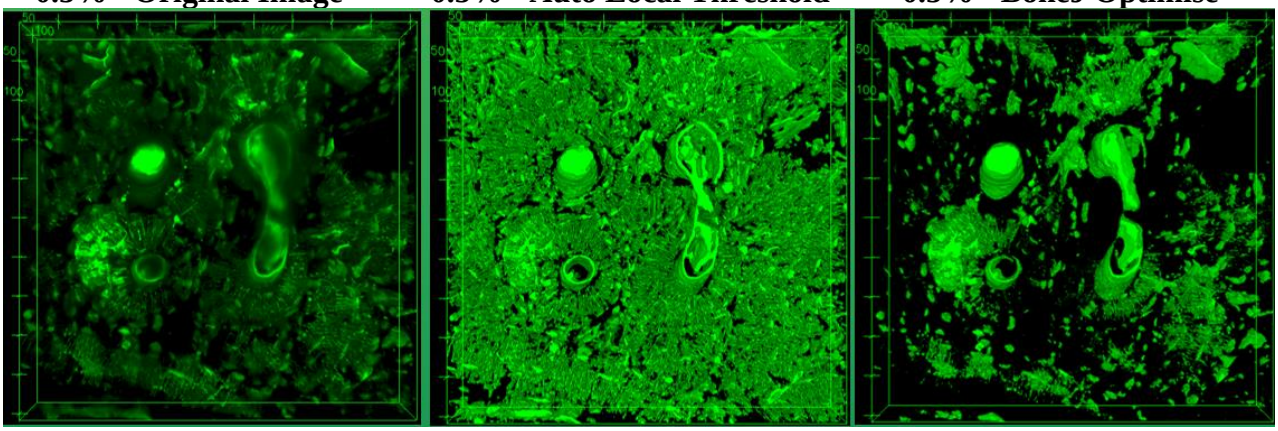

0.4% - Original Image **0.4% - Auto Local Threshold** **0.4% - BoneJ Optimise**

Figure 8: Three-dimensional images with each thresholding method for 0.6% - 0.4% FITC

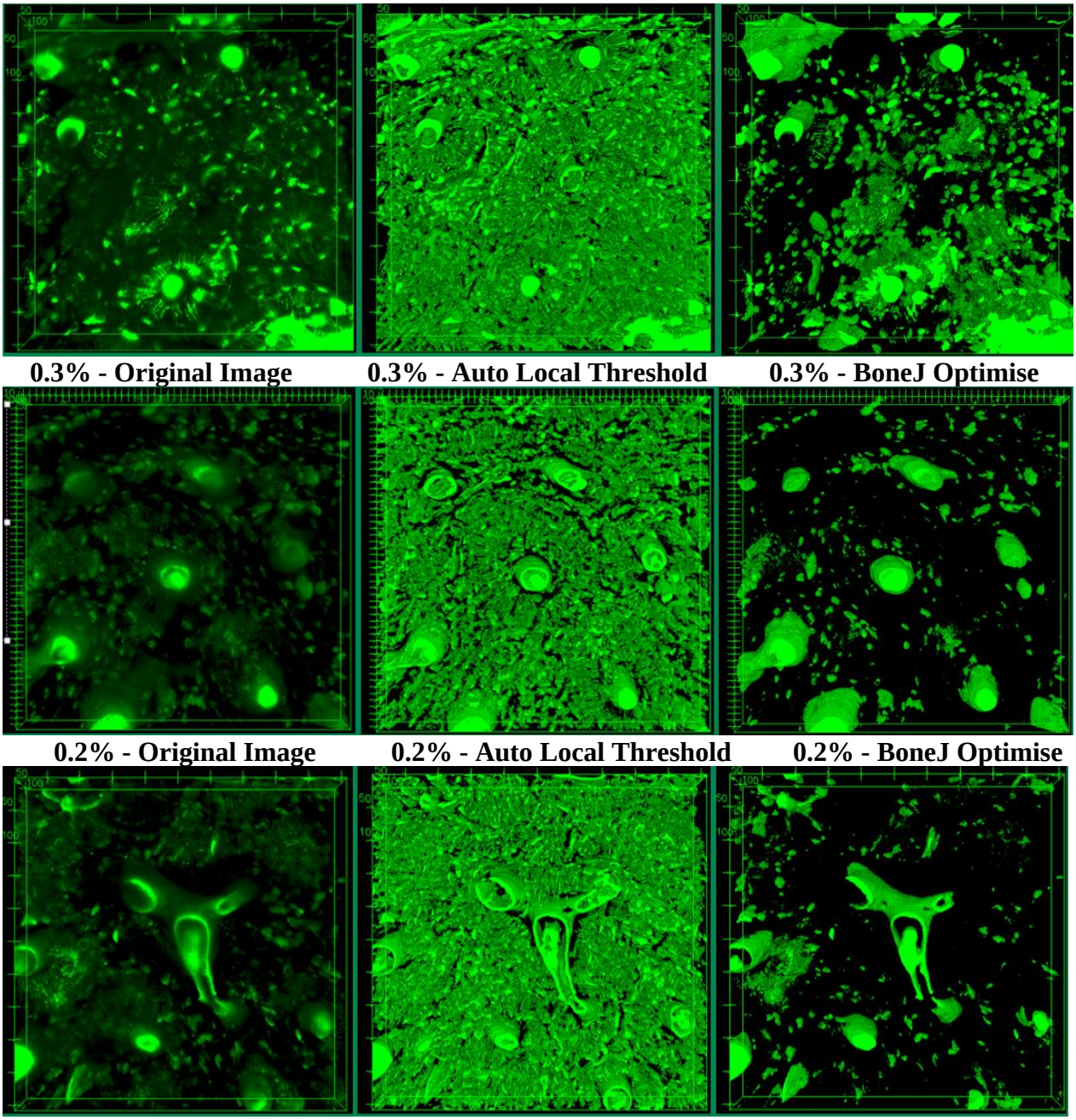

Figure 9: Three-dimensional images with each thresholding method for 0.3% - 0.1% FITC

DISCUSSION AND CONCLUSION

Multiphoton CSLM is an effective tool for visualizing vascular and cellular pore shape and distribution. FIJI also includes tools for segmenting, isolating, and measuring shape

parameters of 3D objects. For example, the tool Segment blob in 3D viewer was used to extract vascular pores from the 0.9% image segmented in BoneJ Optimise (Fig. 10). Skeletonize 3D and Analyze 3D were used to trace the branching pattern of this lacunar-canalicular pore and found a segment with 120 branches and 57 junctions (Fig. 11).

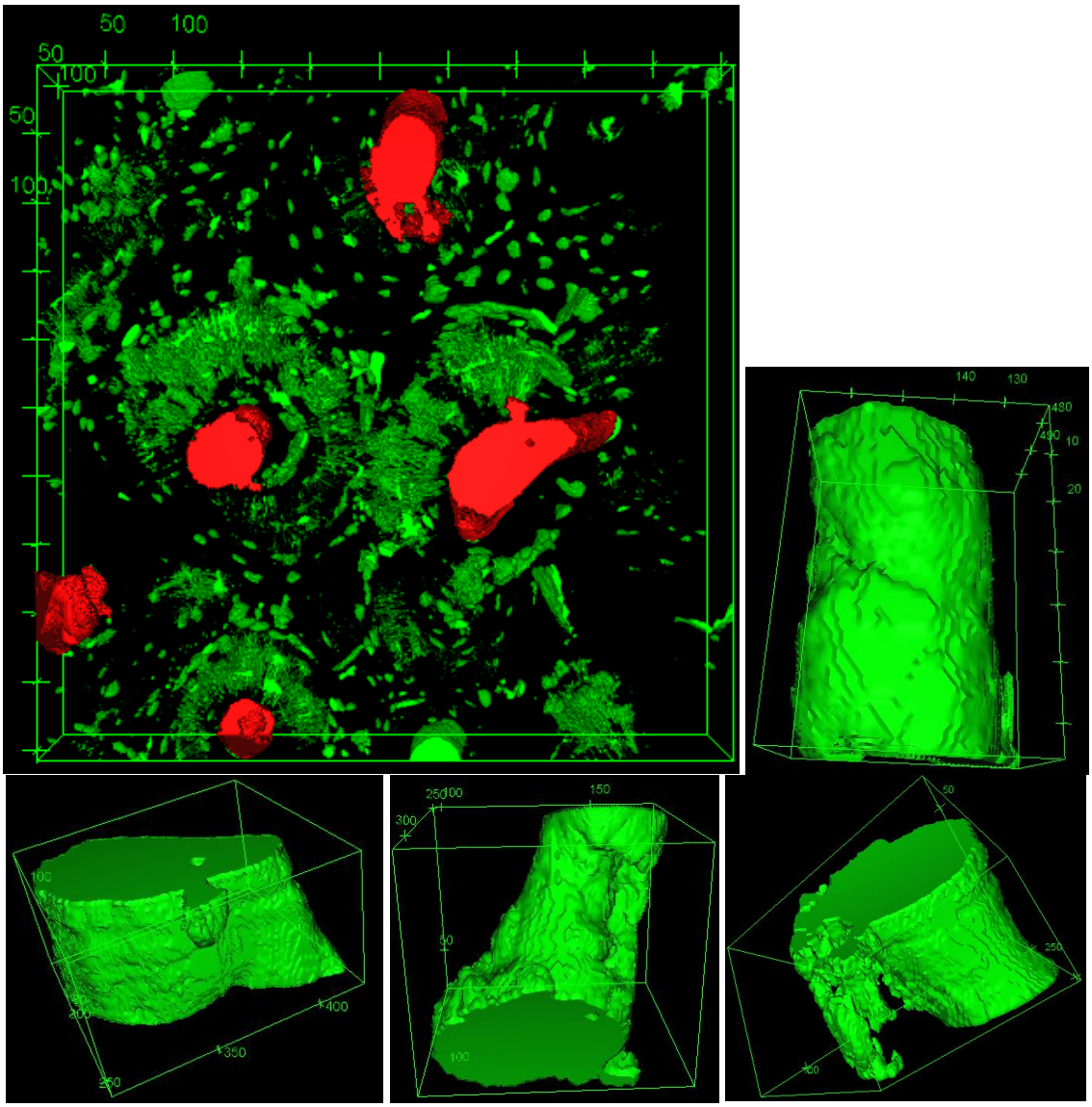

Figure 10: Vascular pores shown in red in the 0.9% FITC three-dimensional image are isolated as three-dimensional structures with the ImageJ tool "Segment Blob in 3D Viewer"

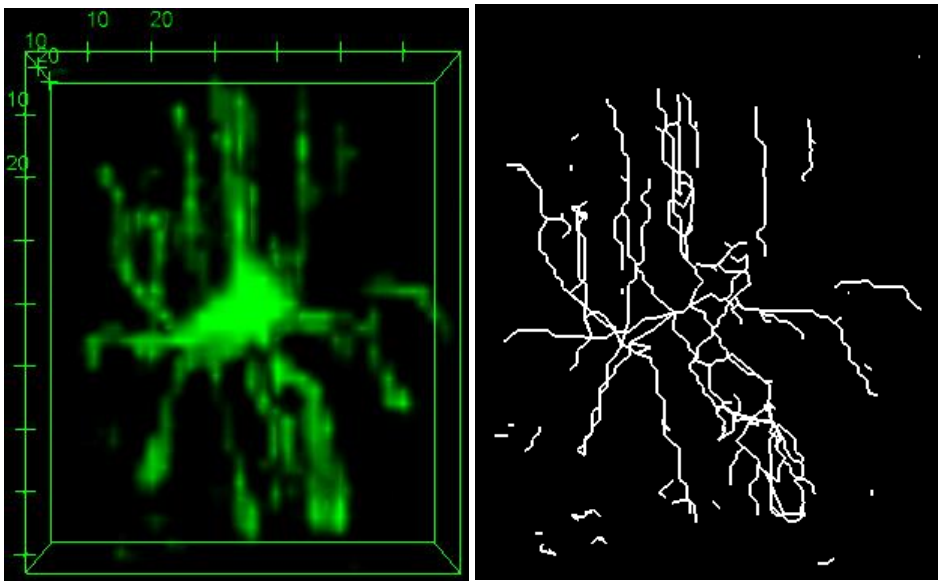

Figure 11: A lacunar-canalicular pore system (left) from the 0.9% FITC three-dimensional image undergoes connectivity analysis (right) with ImageJ Skeletonize 3D and Analyze 3D.

With a high enough FITC stain concentration (0.6%-1%), HV, Offset, and image noise remain low enough for vascular and cellular pore network isolation. Auto Local Threshold is preferable for outlining more complete canalicular networks, while BoneJ Optimise more easily isolates and fills in whole vascular pores. These results demonstrate that the method from Ciani et al.[22] is suitable for three-dimensional imaging of both vascular and cellular pore networks in human bone tissue, with an optimized FITC stain concentration of 0.6 – 1%. Multiphoton confocal microscopy facilitates deep penetrance into the sample to allow quantification of three-dimensional pore structures.

References

1. Zebaze R and Seeman E. 2014. Cortical bone: A challenging geography. J Bone Miner Res 30(1):24-29.
2. McCalden RW, McGeough JA, Barker MB, Court-Brown CM. 1993. Age-related changes in the tensile properties of cortical bone. The relative importance of changes in porosity, mineralisation and microstructure. J. Bone. Joint. Surg. 75-A:1193–1205.
3. Burr DB and Akkus O. 2014. Bone Morphology and Organization. In: Basic and Applied Bone Biology. David B. Burr and Matthew R. Allen, eds. London, UK: Academic Press. pp 3- 25.
4. Agnew AM, Bolte JH. 2012. Bone Fracture: Biomechanics and risk. In: Bone Histology: An Anthropological Perspective. Christian Crowder, ed. Boca Raton, FL: CRC Press.
5. Thomas CD, Feik SA, Clement JG. 2005. Regional variation of intracortical porosity in the midshaft of the human femur: Age and sex differences. J. Anat. 206(2): 115 -125.
6. Zebaze, A. Ghasem-Zadeha, A. Bohtea, A. Iuliano-Burnsa, S., Mackiea, E. Seeman, E. 2009. Age-related bone loss: The effect of neglecting intracortical porosity. Bone 44:S99-S120.
7. Ebacher V, Tang C, McKay H, Oxland TR, Guy P, Wang R. 2007. Strain redistribution and cracking behavior of human bone during bending. Bone 40: 1265 – 1275.
8. Skedros JG, Mason M, Bloebaum R. 1994. Differences in osteonal micromorphology between tensile and compressive cortices of a bending skeletal system: indications of potential strain-specific differences in bone microstructure. Anat. Rec. 239:405–413.
9. Agnew AM and Stout, SD. 2012. Brief Communication: Reevaluating osteoporosis in human ribs: The role of intracortical porosity. Am. J. Phys. Anthropol. 148: 462-466.
10. Bellido T, Plotkin L, Bruzzaniti A. 2014. Bone Cells. In: Basic and Applied Bone Biology. David B. Burr and Matthew R. Allen, eds. London, UK: Academic Press. pp.27 – 46.
11. Carter Y, Suchorab JL, Thomas CD, Clement JG, Cooper DM. 2014. Normal variation in cortical osteocyte lacunar parameters in healthy young males. J Anat 225(3):328-36.
12. Himeno-Ando A, Izumi Y, Yamaguchi A, Iimura T. 2012. Structural differences in the osteocyte network between the calvaria and long bone revealed by three-dimensional fluorescence morphometry, possibly reflecting distinct mechano-adaptations and sensitivities. Biochem Biophys Res Commun. 417: 765–770.
13. Stout SD, Brunsden BS, Hildebolt CF, Commean PK, Smith KE, Tappen NC. 1999. Computer assisted 3D reconstruction of serial sections of cortical bone to determine the 3D structure of osteons. Calcif. Tissue. Int. 65: 280–284.
14. Bell KL, Loveridge N, Reeve J, Thomas CD, Feik SA, Clement JG. 2001 Super-osteons (remodeling clusters) in the cortex of the femoral shaft: influence of age and gender. Anat. Rec. 264: 378–386.
15. Cooper DML, Matyas JR, Katzenberg MA, Hallgrimsson B. 2004. Comparison of microcomputed tomographic and microradiographic measurements of cortical bone porosity. Calcif. Tissue. Int. 74: 437–447.

16. Yin L, Venkatesan S, Webb D, Kalyanasundaram S, Quin Q. 2012. 2D and 3D mapping of microindentations in hydrated and dehydrated cortical bones using confocal laser scanning microscopy. J Mater Sci 47: 4432 – 4438.
17. Smith IO, Ren F, Baumann MJ, Case ED. 2006. Confocal laser scanning microscopy as a tool for imaging cancellous bone. J. Biomed. Mater. Res., Part B 79(1): 185 – 192.
18. Grotz KA, Piepkorn Bm Al-Nawas B, Duschner H, Bittinger F, Kann P, Beyer J, Wagner W. 1999. Confocal Laser Scanning Microscopy: A Nondestructive Subsurface Histotomography of Healthy Human Bone. Calcif Tissue Int 65:8-10.
19. Dechow PC, Dong HC, Bolouri M. 2008. Relationship Between Three-Dimensional Microstructure and Elastic Properties of Cortical Bone in the Human Mandible and Femur. In: Primate Craniofacial Function and Biology. Chris Vinyard, Matthew J. Ravosa, and Christine Wall, eds. New York, NY: Springer Science + Business Media, LLC. pp. 265-293.
20. Maggiano C, Dupras ZT, Schultz M, Biggerstaff J. 2009. Confocal laser scanning microscopy: a flexible tool for simultaneous polarization and three-dimensional fluorescence imaging of archaeological compact bone. J Arch Science 36: 2392 – 2401.
21. Papageorgopoulou C, Kuhn G, Ziegler U, Ruhli FJ. 2010. Diagnostic Morphometric Applicability of Confocal Laser Scanning Microscopy in Osteoarchaeology. Int. J. Osteoarchaeol. 20: 708–718.
22. Ciani C, Doty SB, Fritton SP. 2009. An effective histological staining process to visualize bone interstitial fluid space using confocal microscopy. Bone 44: 1015 – 1017.
23. Sharma D, Ciani C, Marin PA, Levy JD, Doty SB, Fritton SP. 2012. Alterations in the osteocyte lacunar-canalicular microenvironment due to estrogen deficiency. Bone 51(3):488 – 497.
24. Verbruggen SW, Vaughan TJ, McNamara LM. 2012. Strain amplification in bone mechanobiology: a computational investigation of the in vivo mechanics of osteocytes. J R Soc Interface 9(75):2735-2744.
25. Murphy D and Davidson M. 2013. Fundamentals of Light Microscopy and Electronic Imaging. 2nd ed. Hoboken, NJ: Wiley-Blackwell.
26. Saban J, Zussman MA, Havey R, Patwardhan AG, Schneider GB, King D. 1996. Heterozygous oim mice exhibit a mild form of osteogenesis imperfecta. Bone 19(6):575–9.
27. Schindelin J, Arganda-Carreras I, & Frise E. et al. 2012, "Fiji: an open-source platform for biological-image analysis", *Nature methods* 9(7): 676-682.
28. Doube M, Kłosowski MM & Arganda-Carreras I. et al. 2010. "BoneJ: Free and extensible bone image analysis in ImageJ", *Bone* 47(6): 1076-1079.
29. Robling AG, Fuchs RK, Burr DB. 2014. Mechanical Adaptation. In: Basic and Applied Bone Biology. David B. Burr and Matthew R. Allen, eds. London, UK: Academic Press. pp 175 – 203.
30. Frost HM. 2003. Bone's mechanostat: a 2003 update. Anat. Rec. A. Discov. Mol. Cell. Evol. Biol. 275(2): 1081 – 1101.
31. Ruff CB, Larsen CS. 2014. Long bone structural analyses and the reconstruction of past mobility: a historical review. In: Carlson KJ, Marchi D, editors. Reconstructing mobility:

Environmental, behavioral, and morphological determinants. New York, NY: Springer: 13 – 29.
32. Gocha TP and Agnew AM. 2016. Spatial variation in osteon population density at the human femoral midshaft: Histomorphometric adaptations to habitual load environment. J. Anat. 228: 733 – 745
33. Skedros JG, Grunander TR, Hamrick MW. 2005. Spatial Distribution of Osteocyte Lacunae in Equine Radii and Third Metacarpals: Considerations for Cellular Communication, Microdamage Detection and Metabolism. Cells Tissues Organs 180: 215 – 236.
34. Akira. 2006. Diagram of a two-photon excitation microscope. Wikipedia. Retrieved 20 February 2017. https://commons.wikimedia.org/wiki/File:Diagram_of_a_two-photon_excitation_microscope_en.svg.